AIAA JOURNAL
Vol. 55, No. 11, November 2017

Optical Measurements of Transitional Events in a Mach-6 Boundary Layer

Stanislav Gordeyev* and Thomas J. Juliano†
University of Notre Dame, Notre Dame, Indiana 46556

DOI: 10.2514/1.J055759

Results of aero-optical measurements of naturally occurring transitional structures—turbulent spots and second-mode wave packets—in a hypersonic laminar boundary layer are presented. Optical spectra of turbulent spots were similar to spectra for fully turbulent boundary layers, and the average thickness of the boundary layer during the turbulent spot was approximately 50% of the fully turbulent boundary layer. The convective speed of the leading edge of the spot was measured to be 0.95 of the freestream speed, whereas the trailing edge moves at 0.7 of the freestream speed. The dominant frequency of the wave packet structures was about 70 kHz, consistent with the theoretically predicted second-mode frequency; the average convective speed of the packets was measured to be 0.88 of the freestream speed. Using the frozen field hypothesis, the wave fronts were stitched together to reveal streamwise/spanwise topology of the packets. The packets were found to be fairly narrow, about 2–3δ in the spanwise direction, extending for 30–60δ in the streamwise direction.

Nomenclature

a	=	speed of sound
C	=	correlation coefficient
f_{samp}	=	sampling frequency
K_{GD}	=	Gladstone–Dale constant
M	=	Mach number
n	=	index of refraction
OPD_{RMS}	=	spatial rms of optical path difference
P_0	=	stagnation pressure
R	=	tunnel radius
Re_δ	=	Reynolds number, based on U_∞ and δ
t, T, τ	=	time
T_0	=	stagnation temperature
U	=	time-averaged speed
x, y, z	=	spatial coordinates
Δt	=	sampling interval, equal to $1/f_{\text{samp}}$
Δx	=	streamwise separation
δ	=	boundary-layer thickness
θ	=	deflection angle
μ	=	angle of conical wave
ρ	=	density

Subscripts

∞	=	freestream value
C	=	convective
LE	=	leading edge
TE	=	trailing edge

Superscript

‘	=	fluctuating value

Presented as Paper 2016-3348 at the 46th AIAA Fluid Dynamics Conference, Washington, D.C., 13–17 June 2016; received 14 October 2016; revision received 2 May 2017; accepted for publication 12 July 2017; published online 28 August 2017.

*Associate Professor, Department of Mechanical and Aerospace Engineering, Hessert Laboratory for Aerospace Research. Associate Fellow AIAA.

†Assistant Professor, Department of Mechanical and Aerospace Engineering, Hessert Laboratory for Aerospace Research. Senior Member AIAA.

I. Introduction

THE state of a hypersonic boundary layer—whether it is laminar, transitional, or turbulent—is an important factor in the design of hypersonic vehicles due to its effect on surface heating, skin friction, separation, aero-optical distortion, and other boundary-layer properties [1]. Thus, the boundary-layer state's aero-optical impact can be exploited as a means to study the boundary layer. In this experiment, a Shack–Hartmann wave front sensor (WFS), which nonintrusively measures density fluctuations, was used to investigate various transitional events, namely turbulent spots and second-mode instability waves, in a laminar hypersonic boundary layer at high Reynolds numbers.

Aero-optical effects [2,3] are the result of the dependence of the index of refraction, n, on the density of a gas, ρ, via the Gladstone–Dale constant, K_{GD} (which is approximately 2.27×10^{-4} m^3/kg in air for visible wavelengths of light), $n(x, y, z, t) - 1 = K_{\text{GD}}\rho(x, y, z, t)$. Light passing through regions of unsteady turbulent flow is distorted by the spatially and temporally fluctuating density fields present along the optical path. The effect of turbulent density fluctuations on the propagation of light can be quantified by defining the optical path difference (OPD) as the average-removed integral of the index of refraction of a medium along the physical length traversed by a ray of light

$$\text{OPD}(x, y, t) = \int n'(x, y, z, t)\,\mathrm{d}z = K_{\text{GD}} \int \rho'(x, y, z, t)\,\mathrm{d}z$$

where primes denote mean-removed fluctuations and z is the direction of beam propagation.

The present work, which examines the relatively thick laminar boundary layer on a quiet-tunnel nozzle wall, most closely resembles cursory work by Juliano [4] and much deeper study by Casper et al. [5] and Casper [6], which primarily used wall-mounted sensors. Other recent work on disturbance wave packets has primarily employed slender cone models, with thinner boundary layers and correspondingly higher frequencies than the nozzle wall studies. This work includes a spatial direct numerical simulation by Sivasubramanian and Fasel [7], who excited wave packets on a sharp cone by introducing a localized pulse of velocity disturbances. Their flow parameters matched those of an experiment by Casper et al. [8]. Heitmann et al. [9] and Heitmann and Radespiel [10] conducted complementary experiments and simulations, wherein controlled disturbances were introduced into a cone's boundary layer by means of laser-generated plasma. Other studies [7,9,10] all found evidence of two-dimensional (2-D) second-mode waves at the center of the wave packet. The computational studies [7,10] also revealed spherical acoustic waves, which were explained to be vestiges of the boundary-layer forcing.

Jewell et al. [11,12] studied turbulent spots in a hypervelocity flow over a cone with fast-response thermocouples. Fiala et al. [13] used thin-film heat-flux gauges on a blunt cylinder to make similar measurements in a gun tunnel.

Whereas most prior experimental studies have used surface-mounted sensors, some have used optical techniques, which offer fast response times and are nonintrusive. Casper et al. [14,15] and Laurence et al. [16] employed high-speed schlieren techniques to obtain side views of developing wave packets and turbulent spots. The WFS used in the current study provides a planform view of boundary-layer disturbances, thereby complementing the high-speed schlieren technique. Furthermore, the WFS offers several advantages over wall-mounted sensors. The interrogation region can be smaller than that of a typical pressure transducer and multiple optical sensors can be clustered more tightly than physical transducers. Additionally, the boundary-layer density fluctuation spectrum can be assessed simultaneously with the wall shear stress or unsteady pressure. One WFS can replace several individual transducers for the measurement of convective speeds and directions of density fluctuations, thus a priori knowledge of the disturbances to optimize sensor layout is avoided. Also, the nonintrusive nature of aero-optical measurements makes them very attractive to study transitional hypersonic boundary layers, which generally are very sensitive to any surface defects [17].

Although the aero-optics of turbulent boundary layers has been extensively studied in recent years ([2,18] and references therein), including experimental measurements [19–23] and numerical simulations [24–26] in high supersonic and hypersonic turbulent boundary layers, aero-optical measurements of transitional events in laminar boundary layers at high speeds are limited and many important questions about the details of the dynamics and topology of underlying structures remain unanswered. The highly spatially and temporally resolved optical data yielded by the Shack–Hartmann WFS can provide valuable quantification of the amplification and propagation of disturbances within a transitional boundary layer.

II. Experimental Setup

The data presented herein were collected in the Boeing/AFOSR Mach-6 Quiet Tunnel (BAM6QT) at Purdue University. Quiet wind tunnels are so named because of their comparatively low noise level, defined here as rms pitot-pressure fluctuations normalized by the mean pitot pressure. While running quietly, the noise level is less than 0.05%, and increases to about 3% when noisy [27]. Hypersonic wind tunnels achieve quiet flow by maintaining laminar nozzle-wall boundary layers [28]. The BAM6QT employs many features to this end (Fig. 1). The valve in the bleed-slot suction plumbing can be set to open or remain closed during a run, permitting the user to control whether the nozzle-wall boundary layer is laminar (for quiet flow) or turbulent (noisy flow). A more comprehensive discussion of the components of the BAM6QT is contained in [4].

The air is heated to a nominal stagnation temperature of 433 K, corresponding to a static temperature of 53 K when expanded to Mach 6. The freestream Mach number in the test section is 6.0 under quiet flow and varies slightly with stagnation pressure. Thicker, turbulent nozzle-wall boundary layers reduce the freestream Mach number to 5.8 when running with conventional noise levels.

The BAM6QT test section accommodates several interchangeable inserts [29]. For these tests, two windows with 4-cm viewable diameters were installed at an axial station 1.924 m from the nozzle throat in the forward ports of the 75×250 mm window inserts [30], as shown in Fig. 1.

Several runs with different stagnation pressures were performed (Table 1). All runs were performed under the quiet tunnel regime. The initial T_0 was 433 K (160 °C) for all runs. For the range of stagnation temperatures, the freestream speed was approximately 870 m/s. Runs B2, B4, B6, and B8 contain two independent runs under the same conditions to increase the sampling time. Using laminar boundary-layer simulations, reported in [31], for stagnation pressures between 50 and 150 psi, the laminar boundary thickness was extrapolated to be 5.6 mm for all runs. Reynolds number per unit length was 13.5 M/m, giving $Re_\delta = 75{,}800$.

All measurements were performed using a high-speed Shack–Hartmann WFS. This WFS is capable of measuring wave fronts with a spatial resolution up to 70×60 points with an absolute accuracy better than 0.01 μm and sampling rates up to 1 MHz. A schematic of the experimental setup is shown in Fig. 2. The laser beam was expanded to 40 mm in diameter and passed perpendicularly through two flat windows mounted in the test section. When passed through the test section, the laser beam encountered two hypersonic boundary layers, one on each side of the test section. After reflecting from the return mirror, the beam traversed back to the optical table exactly the same way it came, the so-called double-pass experiment. In this arrangement, the beam travels through the region of interest twice, increasing the wave front amplitude by a factor of two. The returning beam was split off using a cube beam splitter, contracted to a 12.5 mm diameter using a contracting telescope, and finally sent to a Phantom v1611 high-speed digital camera. The camera had a 38 mm focal length, 70×60 lenslet array with 0.3 mm pitch attached to it. After passing through the lenslet array, the beam was split into subaperture beams and focused on the camera sensor, creating a series of dots. The distance between dots, projected to the window insert, defines the spatial resolution of the measured wave fronts, which was approximately 1 mm. To collect the wave fronts over the entire aperture with the spatial resolution of 37 subapertures in each direction, the sampling rate was reduced to 30,000 Hz in run B2. To achieve the high sampling rate of 1,000,000 fps, only a small, 128×16 pixel portion of the image, corresponding to a single line of 11 subapertures, was sampled for 4 s for runs A8 and A11 (Fig. 3). Finally, wave fronts were collected at 531,645 Hz for runs B4 and B6 and at 250,000 for run B8 with proportionally reduced aperture sizes.

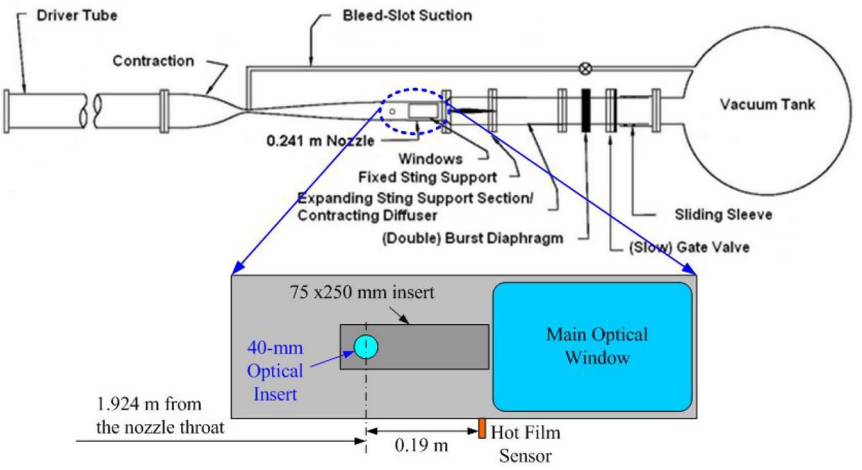

Fig. 1 BAM6QT schematic with a diagram of the test section.

Table 1 Initial flow parameters and test conditions

Run number	P_0, psi	Aperture size, mm	Aperture location	Sampling frequency, Hz
A8	175	9.5×1.2	10 mm above centerline	1,000,000
A11	170	9.5×1.2	14 mm above centerline	1,000,000
B2	175	35 mm diameter	centerline	30,000
B4	174	11.4×5.7	centerline	531,645
B6	174	11.5×5.7	10 mm above centerline	531,645
B8	175	22.9×11.5	centerline	250,000

As mentioned previously, the beam goes through two boundary layers, one on each side of the tunnel. It cannot distinguish in which boundary layer an individual event occurs. If the turbulent boundary layer is present over the entire circumference of the tunnel at the measurement station, the parts of the boundary layer over both window inserts can be assumed to be statistically the same and independent. In this case, the statistically averaged square of the wave front amplitude (and a power spectrum) is a sum of the statistically averaged squares of the wave front amplitudes (or power spectra) from two individual boundary layers [32]. Thus, the statistics of the single boundary layer can be extracted from statistics of the two-boundary-layer wave fronts. If a spatially localized dynamical structure is present over one of the windows, wave fronts provide spatiotemporal information about this structure regardless of on which side of the tunnel it is located. As will be shown later in this paper, these localized structures occur quite infrequently, so the probability of these structures being present simultaneously over both inserts is very small.

Simultaneously with aero-optical measurements, local heat transfer information was collected by a Senflex hot film sensor mounted at the bottom of on the nozzle wall 190 mm downstream of the beam location (see Fig. 1). It was controlled by a Bruhn-6 constant-temperature anemometer and sampled at 1000 kHz for the duration of each run. These sensors are uncalibrated and customarily used to verify qualitatively the condition of the nozzle-wall boundary layer (laminar, turbulent, or separated). A Kulite pressure transducer flush-mounted to the contraction inlet provided the stagnation pressure during the run. A Tektronix digital oscilloscope in Hi-Res mode was used to record the output voltages of the hot films and Kulite.

Several runs, including B8, were performed with the aperture center aligned with the centerline of both inserts. In this case, there was a minimized step between the flat windows and the contoured tunnel wall upstream of the measurement location. To study a possible effect of the upstream step on the boundary layer structure, the sampling area was shifted 10 mm in the spanwise direction for runs A8 and B6, so a small backward-facing step of approximately 0.4 mm, or 7% of the laminar boundary-layer thickness, was present upstream of the measurement location, potentially perturbing the boundary layer over the flat inserts. Finally, the sampling area had been shifted by 14 mm in the spanwise direction during run A11, so it was situated downstream of a larger backward-facing step of 0.8 mm, or 14% of the laminar boundary-layer thickness.

III. Data Analysis

For each run, temporal evolutions of the dots' centroids were extracted using in-house software and converted into time-series deflection angles for each subaperture beam. These measurements are essentially equivalent to measurements using a multibeam Malley probe [18,21]. The deflection-angle time series was used to identify the transitional events using various pattern-recognition techniques, described next. The deflection angles are local gradients of the wave front, so they were used to reconstruct the spatial-temporal 2-D wave front sequences for the large apertures (runs B2, B4, and B6) using the Southwell method [33]. For these runs, instantaneous tip/tilt and piston modes were removed from each wave front. To eliminate the corrupting effect of the tunnel vibrations, a moving averaging filter with the duration of 0.2 ms was also applied to the wave front sequences.

To compute speeds of aero-optical distortions for runs A8, A11, B4, and B6, the deflection angles at different points over the aperture were cross-correlated at various time delays. Determining a local maximum in the correlation

$$C(\Delta x, \tau) = \left\langle \int \theta(x,t)\theta(x+\Delta x, t+\tau)\,\mathrm{d}x \right\rangle, \qquad \max(C) \to \tau(\Delta x)$$

gives measurements of the convective speed as a best-fit slope between Δx and $\tau(\Delta x)$. Here, angled brackets denote ensemble averaging over all possible pairs of points with the fixed streamwise separation Δx.

For run B8, a similar technique was used, but this time, a correlation between two sequential frames was computed

$$C(\Delta x, \Delta t; T) = \int \theta(x,T)\theta(x+\Delta x, T+\Delta t)\,\mathrm{d}x, \quad \max(C) \to \Delta x$$

where $\Delta t = 1/f_{\text{samp}}$ is a time interval between two frames, and the convective speed at the given time T was computed as $U_C(T) = \Delta x/\Delta t$.

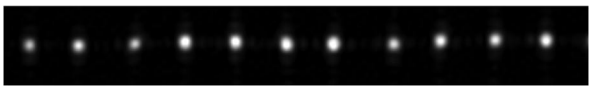

Fig. 3 A 16×128 wave front image for runs A8 and A11.

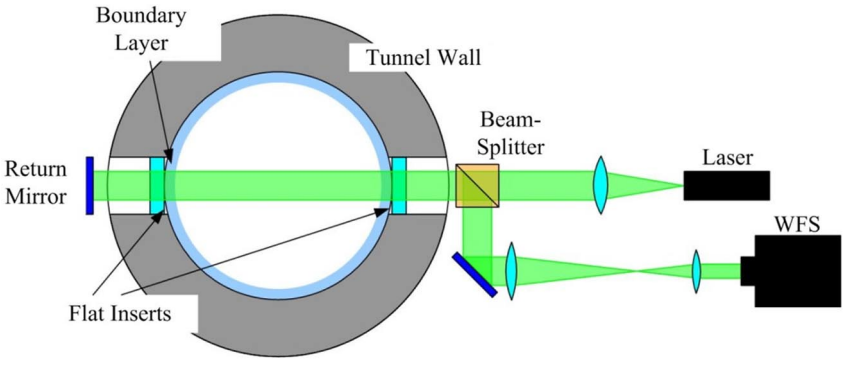

Fig. 2 Schematics of boundary layer experimental setup.

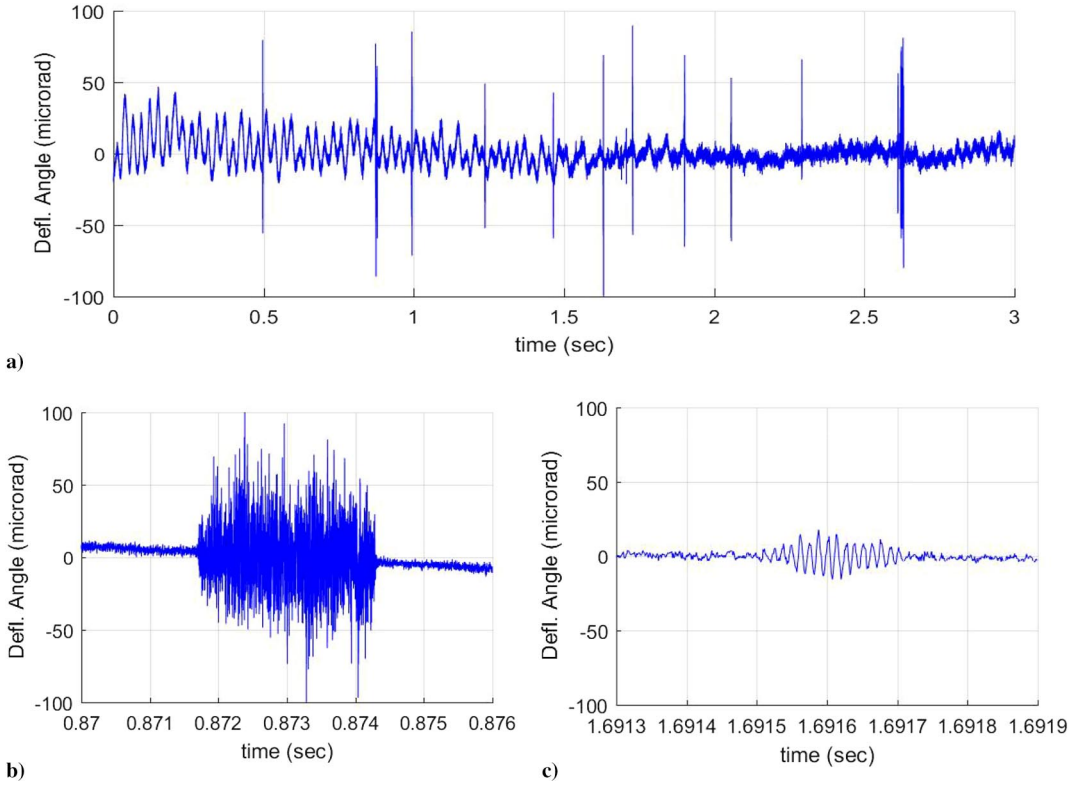

Fig. 4 Illustrations of a) long time series of the deflection angle for run A8, b) expanded time series showing a localized broadband increase associated with the turbulent spot, and c) a narrowband event corresponding to the second mode.

IV. Results

Analysis of previously collected aero-optical data [23] and unsteady surface pressures [5] in the BAM6QT had shown that the boundary layer is fully laminar for stagnation pressures below 140 psi. Above this pressure, the freestream Reynolds number becomes large enough to cause intermittent transitional events in the laminar boundary layer [5]. A representative example of deflection-angle time series is presented in Fig. 4a. For most of the time, the deflection angle exhibits only low-frequency, tunnel-vibration-related decaying oscillations, indicating that the boundary layer was laminar during the most of the run. However, at several instances, the time series exhibit intermittent, short-lived increases in the deflection angle amplitude. A close inspection of the time series revealed the presence of two types of the transitional events. The first one, shown in Fig. 4b, indicated the presence of a brief turbulent spot. The second one, shown in Fig. 4c, appeared to be an even-shorter-lived narrowband wave packet event, which is suspected to be a transitional second-mode-instability wave packet.

A. Turbulent Spots

Turbulent spots, or bursts, are characterized by broad-spectrum fluctuations typical of a turbulent boundary layer (Fig. 4b). This flow feature is well-known and was observed and documented in this tunnel by other researchers [4–6]. To study the statistics of the turbulent spots, time periods with either large spatial (run B2) or large temporal (runs A8, A11, B4, B6, and B8) wave front fluctuations were extracted from wave front sequences; a total of 373 turbulent-spot events were extracted from all runs. For each event, the event duration was determined and the probability distribution was computed (Fig. 5). The average turbulent-spot duration was found to be about 1.42 ms. The shortest event was of 1.15 ms duration and the longest one was 1.8 ms; 75% of the durations were found to be between 1.3 and 1.5 ms. Later in this paper, it will be shown that this duration is consistent with the notion that these large turbulent spots originate near the nozzle throat, as suggested in [5].

Time series during the turbulent spots for runs A8 and A11 were used to calculate the deflection angle spectrum, which is presented in

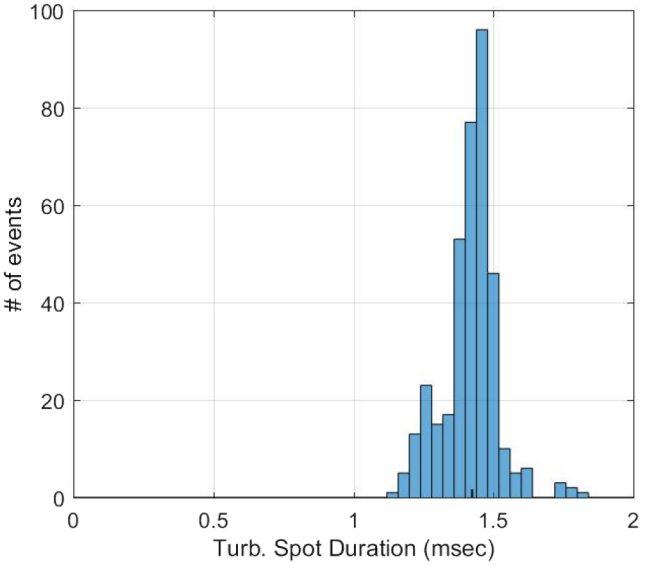

Fig. 5 Statistics of the turbulent spot duration at the measurement station.

Fig. 6 (red line). Comparison with the fully turbulent boundary-layer spectrum [23], represented by a black thick line in Fig. 6, indicated that the temporal statistics of turbulent spots is quite similar to a fully turbulent boundary layer. The turbulent-spot spectrum has a slightly larger optical energy in the high frequencies above 200 kHz and possibly lower energy between 20 and 40 kHz. Unfortunately, using less than 400 events precludes having a well-converged spectrum and additional measurements are required to obtain more events and to improve the accuracy of the spectrum calculation.

The comparison of the deflection-angle time series with the hot film sensor mounted on the bottom of the tunnel wall 0.19 m downstream of the measurement station revealed that this turbulent spot was present simultaneously on the bottom and both sides of the

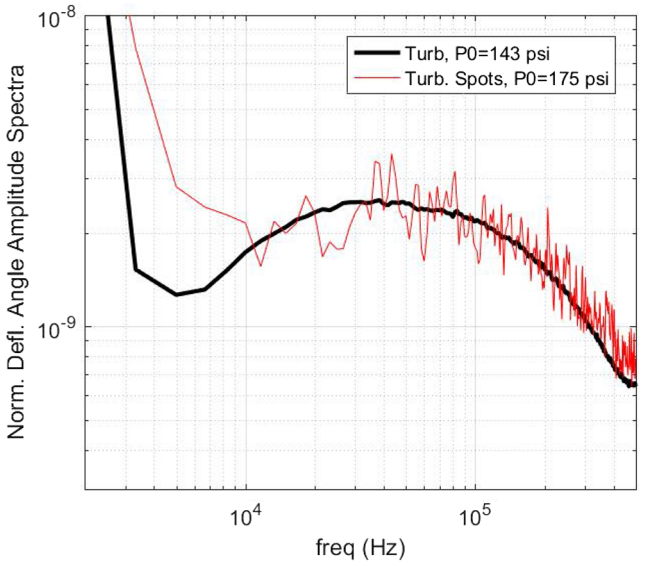

Fig. 6 Comparison between the deflection angle spectra for the fully turbulent boundary layer [23] and during the turbulent spot. Both spectra are normalized by the freestream density.

tunnel (Fig. 7). It indicates that large turbulent spots may engulf the full tunnel circumference at the measurement location, an observation consistent with the conclusion drawn in [5].

In [5], the speeds of both the leading and the trailing edges of the turbulent spots were directly measured using a series of unsteady pressure sensors placed between 2.2 and 2.8 m from the nozzle throat. Note that the leading and trailing edges of the spot are the downstream and upstream edges, respectively. The leading-edge speed was found to be approximately $0.93U_\infty$. Using this convective speed, the time delay for the leading edge of the turbulent spot to travel the distance of 0.19 m from the optical measurement location to the hot film location is 0.235 ms. The beginnings of the turbulent spots in Fig. 7 are marked by vertical dashed-dotted lines. The dotted lines are offset by this 0.235-ms delay, indicating when the turbulent spot should appear over the hot film sensor. In general, the agreement between the predicted and the actual beginning of the turbulent spot is good. In some cases, the spot arrived at the hot film slightly faster (Fig. 7c) or slightly later (Fig. 7d). This variation in the arrival time may be because the leading edge of the turbulent spot is not fully axisymmetric, with some portions of it advanced or delayed; another possible explanation is slightly different convective speeds between the cases.

In Fig. 7, the leading edges in both the deflection angle and in the hot-film time series are easily identifiable. Unlike the trailing edge in the deflection angle series, the trailing edge in the hot-film series does not have a sharp end. Turbulent spots have been found to have relatively distinct leading edges, but long tapered tails; see, for example, [34], Fig. 3 or [13], and Fig. 21. It appears the WFS is not sensitive enough to catch the tail, in which the relatively weak disturbance is concentrated very close to the wall, where the hot film can discern it. Krishnan and Sandham [34] show that the tail's structure is elongated in the streamwise direction, which would not be detected by a streamwise arrangement of wave front measurement volumes, which are sensitive to streamwise density gradients.

The wave fronts over the full aperture were measured during run B2 and the spatial rms of the OPD, denoted $\mathrm{OPD}_{\mathrm{RMS}}(T)$, were computed at different moments during the turbulent spots. A total of 31 turbulent-spot events were analyzed. The ensemble-averaged $\mathrm{OPD}_{\mathrm{RMS}}$, normalized by the time-averaged $\mathrm{OPD}_{\mathrm{RMS}}$ of the fully turbulent boundary layer, are presented in Fig. 8 as a function of normalized time (wherein zero corresponds to the leading edge of the

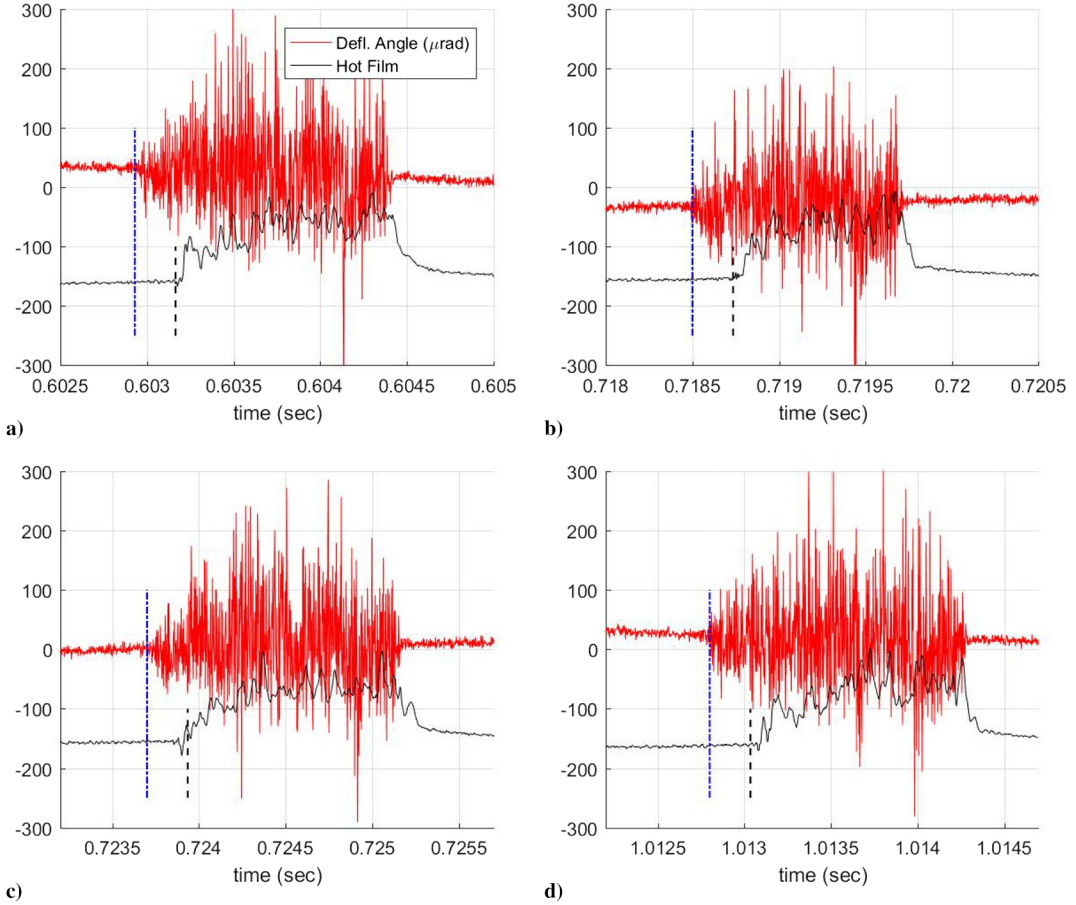

Fig. 7 Four examples of simultaneous optical (deflection angle) and hot film signals. Dashed-dotted lines indicate the beginning of each turbulent spot in the deflection-angle time series and dashed lines are delayed from the beginnings of the turbulent spot by 0.235 ms.

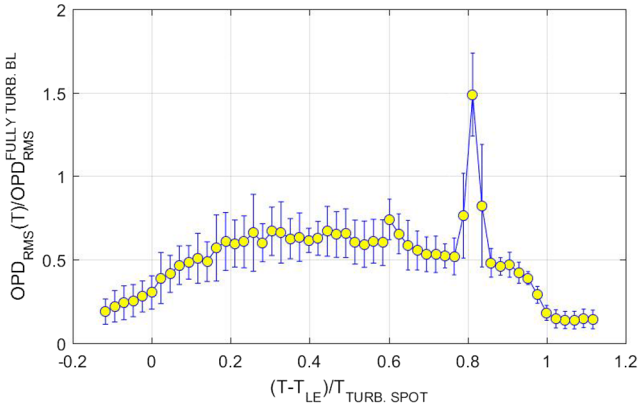

Fig. 8 Ensemble-averaged $OPD_{RMS}(T)$ divided by time-averaged OPD_{RMS} for the fully turbulent boundary layer, as a function of the normalized time during the turbulent spot. Error bars denote standard deviations inside each ensemble.

turbulent spot and one corresponds to the trailing edge of the turbulent spot). Error bars denote standard deviations inside each ensemble. Optical distortions increase during the first 30% of the spot duration and reach a normalized value of 0.65. After that, the normalized value of OPD_{RMS} starts decreasing, except for the sharp increase around the normalized time of 0.8, which will be discussed later. For the same freestream density, OPD_{RMS} is proportional to the local boundary-layer thickness [18], meaning that the turbulent spot reaches its maximum thickness of approximately 65% of the thickness of the fully turbulent boundary layer around the normalized time of 0.3 and monotonically decreases after that. Qualitatively, it agrees with the results of numerical simulations of the turbulent spot evolution at $M = 6$, although the simulations were performed at earlier stages of the turbulent spot evolution [34]. On average, the turbulent spot is approximately half as thick as the turbulent boundary layer.

The deflection angles over the aperture for run B8 were spatially cross-correlated between the adjacent frames to compute the local convective speed of the turbulent structures, U_C, of the different moments during the turbulent spot. Ensemble-averaged results for 12 turbulent-spot events, normalized by the freestream speed, are shown in Fig. 9 as a function of the normalized time relative to the leading edge during the turbulent-spot event. The convective speed of the structures inside the turbulent spot is approximately $0.95U_\infty$ during the first 40% of the turbulent spot duration and starts decreasing after that, reaching values of approximately $0.92U_\infty$ by the end of the turbulent spot.

The speed exhibits an unexpected sharp drop to $0.75U_\infty$ around the normalized time of 0.8, coinciding with the sudden increase in

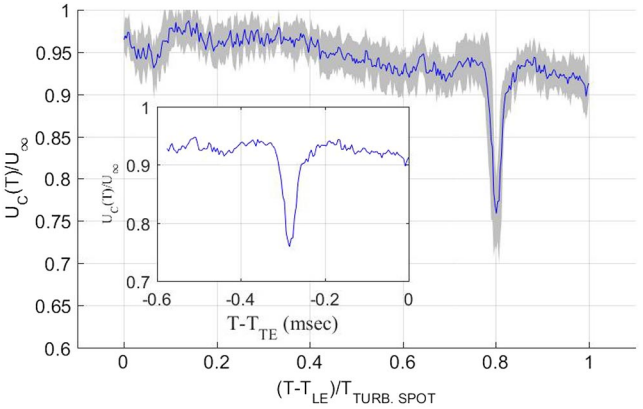

Fig. 9 Ensemble-averaged convective speed, $U_C(T)$, normalized by the freestream speed, as a function of the normalized time relative to the leading edge during the turbulent spot. Gray region denotes standard deviations inside each ensemble and inset shows normalized convective speed as a function of time, relative to the trailing edge arrival.

OPD_{RMS} value, shown in Fig. 8. Analysis of the convective speed calculated for all studied events revealed that the time of the speed drop is always correlated with the arrival of the trailing edge, and both the OPD_{RMS} increase and the convective speed drop occur 0.284 ms before the passage of the trailing edge of the turbulent spot (Fig. 9 inset). This anomalous behavior in the optical levels and the convective speeds can be explained by considering a turbulent spot moving within the axisymmetric tunnel. The turbulent spot is thicker than the surrounding laminar boundary layer, so the change in the displacement thickness between the laminar and the turbulent boundary layer will change the fluidic surface. If the relative speed between a spot's leading (or trailing) edge and the freestream flow is larger than the speed of sound, a moving Mach wave will appear; these waves have been observed in shadowgraph pictures of turbulent spots on a cone [35]. As the turbulent spot was found to be approximately axisymmetric [5], the moving Mach wave is approximately conical, as schematically shown in Fig. 10a. The conical Mach wave is generated by the trailing edge, so it will also travel at the same speed as the trailing edge. Aero-optical distortions are the largest at the tip of the conical shock; when this region of the increased aero-optical distortions passes over the laser beam, overall aero-optical distortions will increase, as observed in Fig. 8 around the normalized time of 0.8. The inspection of the full-aperture wave front at the moment of the largest optical distortions shows evidence of the wedge-type wave front due to the tip of the conical Mach wave (representative wave front in Fig. 10, right).

Knowing the time delay between the arrival at the measurement station of the tip of the conical wave and the trailing edge of the turbulent spot, the speed of the conical wave and, consequently, the speed of the trailing edge can be computed for a given tunnel diameter and the freestream speed. The angle of the moving conical wave, μ, denoted in Fig. 10a, is related to the relative speed between the freestream and the trailing edge speeds

$$\sin(\mu) = \frac{a_\infty}{U_\infty - U_{TE}} = \frac{1}{M_\infty(1 - U_{TE}/U_\infty)}$$

The distance between the trailing edge and the tip of the wave, L, is $L = R\tan(\mu)$, where $R = 0.1205$ m is the tunnel radius. Finally, the time delay is related to this distance as $T_{delay} = L/U_{TE} = 0.284$ ms. Solving all of these equations gives $U_{TE}/U_\infty = 0.71$ and $\mu = 34.6$ deg. This value of the speed for the trailing edge generally agrees with the value of $U_{TE}/U_\infty = 0.67$, obtained by analyzing the time traces of the unsteady wall pressures in this tunnel [5].

Table 2 is a summary of turbulent spot leading-edge and trailing-edge convective speeds reported by other research groups [36–39]. Both experimental and computational results are included. This table is adapted from Table 2 in [11] with some additional details and new results since 2012. The speeds from Table 2 are also plotted in Fig. 11 as a function of M_{edge}. As seen in Fig. 11, the leading-edge convective speed is correlated to the edge Mach number—all tests with edge Mach numbers between 5 and 6 indicate a leading-edge convective speed between 89 and 96% of the freestream velocity, regardless of geometry or data source (experiment or computation). The range of measured trailing-edge convective speed is much larger and does not appear to be correlated to boundary-layer-edge Mach number (Fig. 11).

Note that the convective speed of the turbulent structures near the end of the spot, as shown in Fig. 9, is not necessarily the speed of the trailing edge of the spot, because the spot increases its length in time [5]. When the laser beam travels through both the faster-moving turbulent structure in the turbulent spot on the tunnel wall and the slower-moving tip of the conical shock (which moves at the speed of the trailing edge) in the middle of the tunnel, the wave front represents the integrated value of the aero-optical distortions. As a consequence, the resulting measured convective speed should be in between these speeds, which explains why the minimum optically detected speed in Fig. 9 is only 0.76 of the freestream speed.

As a final remark, as the speed of the leading edge is about 0.95 of the freestream speed, the relative speed is subsonic and, therefore, the leading edge does not generate the Mach wave.

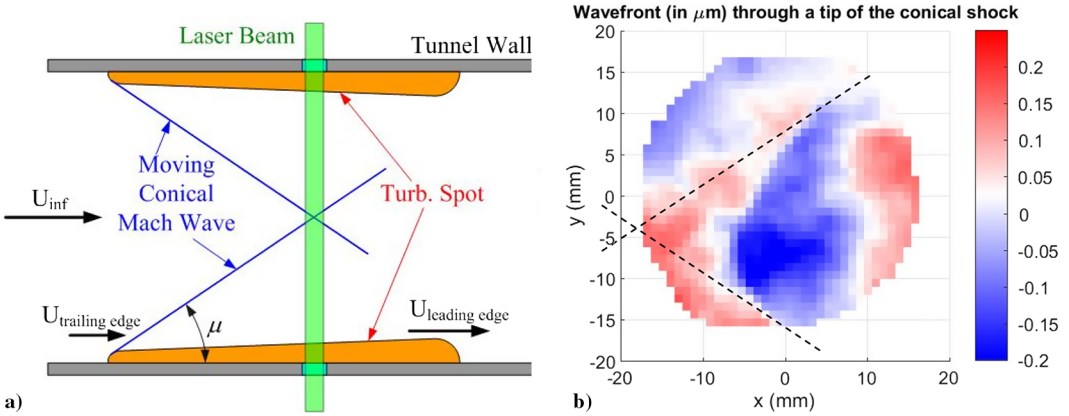

Fig. 10 a) Schematic of a moving axisymmetric turbulent spot and its attached conical Mach wave, generated by a mismatch between the displacement thicknesses. b) A representative wave front, corresponding to the increase in aero-optical distortions in Fig. 8. A wedge-type structure, corresponding to the tip of the conical wave, is clearly seen. The dashed lined indicates the expected boundary of the conical wave.

Knowing that the leading and trailing edges of the turbulent stop move at different speeds (0.95 and 0.71 times the freestream speed, respectively), traveling times from the throat through the nozzle to the measurement station can be calculated (Fig. 12). The difference between the two arrival times at the measurement station was found to be approximately 1 ms. This corresponds to the lower bound of the time duration of the turbulent spot, as the turbulent spot moves at slower relative speeds of 0.9 for the leading edge and 0.6 for the trailing edge at smaller Reynolds numbers (or, equivalently, closer to the nozzle throat). These relative values of the convective speeds give an upper bound of the turbulent-spot duration of 1.4 ms. These estimated values of the turbulent spot duration are very close to the experimentally observed ones in Fig. 5, further indicating that the turbulent spot originates in the tunnel throat and eventually engulfs the whole nozzle circumference by the time it reaches the measurement station 1.9 meters downstream of the nozzle throat.

B. Transitional Second Mode

Another transitional event observed in the laminar boundary layer at high Reynolds numbers is shown in Fig. 4d, with additional deflection-angle time traces shown in Fig. 13. These events correspond to a narrowband wave packet, fundamentally different than the turbulent spots discussed previously. Analysis of the time series has shown that the duration of the single mode is typically between 0.1 and 0.2 ms, or $12–25\delta/U_\infty$. Occasionally, several events appear to combine, resulting in a longer time series. See, for example, the topmost time series in Fig. 13. These events are more spatially localized than the turbulent spots, indicating that the source of origin of the wave packets most probably is located shortly upstream of the measurement station.

Several narrowband structures were observed in each run. As the duration of the recorded data was about 1 s, while each structure was present for only a fraction of a millisecond, the probability of this structure occurring over the window is less than 0.1%. Consequently, the probability of these structures to simultaneously appear over both window inserts is less than one-millionth and can be ignored.

Deflection-angle spectra computed for several of these events are shown in Fig. 14, along with the laminar-boundary-layer spectrum for comparison. These narrowband events were found to have a range of frequencies between 65 and 80 kHz, corresponding to the second (Mack) mode with the frequency of $0.5U_\infty/\delta \sim 70$ kHz [5,31], indicated as a dashed line in Fig. 14.

Runs A8, B4, and B6 were used to compute the convective speed of the second-mode events using the correlation-based method outlined previously. An example of one event's delayed arrival at each spatial point in the aperture is shown in Fig. 15a. A linear fit through the points gives a corresponding convective speed of 785 ± 15 m/s. Analysis of 17 second-mode events for 0.4-mm step (runs A8 and B6), with the distribution shown in light blue in Fig. 15b, allows an estimated convective speed of $U_C = 756 \pm 8$ m/s (90% confidence) or $U_C/U_\infty = 0.87 \pm 0.01$. Only four events were found along the centerline with no step (run B4), with the distribution in dark blue in Fig. 15b. Along the centerline, an estimated convective speed was $U_C = 782 \pm 32$ m/s (90% confidence) or $U_C/U_\infty = 0.90 \pm 0.04$. Using these convective speeds, the average wavelength of the second mode was found to be 10.4 mm or 1.86δ.

Knowing the spatial wavelength of the second mode, a conditional search for all wave front spatial-temporal sequences corresponding to this spatial wavelength was performed for run A2. This run was selected because the wave fronts were sampled over the largest aperture, $\sim 6\delta$. When an event was detected over the aperture for several sequential frames, an instantaneous frozen field hypothesis was used to "stitch" the wave fronts into a pseudospatial "snapshot" of the narrowband structure [40]. Briefly, in the stitching method, the first wave front is fixed and the next wave front is spatially shifted

Table 2 Summary of convective speeds of turbulent spots at hypersonic speeds

Reference	Geometry, type	M_∞	M_{edge}	Re_∞, 10^6/m	Re_{edge}, 10^6/m	U_{edge}, m/s	T_w/T_e	U_{LE}/U_e	U_{TE}/U_e
Zanchetta [36][a]	5 deg cone experimental	9.0	8.02	55.0			4.38	0.98	0.68
Mee [37]	Flat plate experimental	6.1	6.1	4.9	4.9	3370	0.371	0.90 ± 0.10	0.50 ± 0.10
Fiala et al. [13][a]	Blunt cylinder, experimental	8.9	3.74	47.4	2.69[b]	1300[b]	0.97[b]	0.81	0.40
Krishnan and Sandham [34][a]	Flat plate computational	6.0	6.0				7.0	0.89	0.53
Jocksch and Kleiser [38][a]	Flat plate computational	5.0	5.0				5.19	0.96	0.54
Jocksch and Kleiser [38][a]	Flat plate computational	5.0	5.0				1.0	0.89	0.23
Sivasubramanian and Fasel [39]	7 deg cone computational	6.0	5.35	11.0		860[b]	4.66[b]	0.93[b]	0.83[b]
Jewell et al. [11,12]	5 deg cone experimental	5.5[b]	5.11		7.42	3875	0.195	0.96 ± 0.07	0.55 ± 0.07
Heitmann et al. [9]	7 deg cone experimental	5.9	5.3[b]	5.75		860	4.8[b]	0.95	0.75
Casper et al. [5]	Nozzle wall experimental	6.0	6.0	10.8	10.8	870[b]	5.7[b]	0.96	0.73
Gordeyev and Juliano, Present Studies	Nozzle wall experimental	6.0	6.0	13.5	13.5	860	5.68	0.95	0.71

[a]Source: Table 1 in [11].
[b]Derived from reported values.

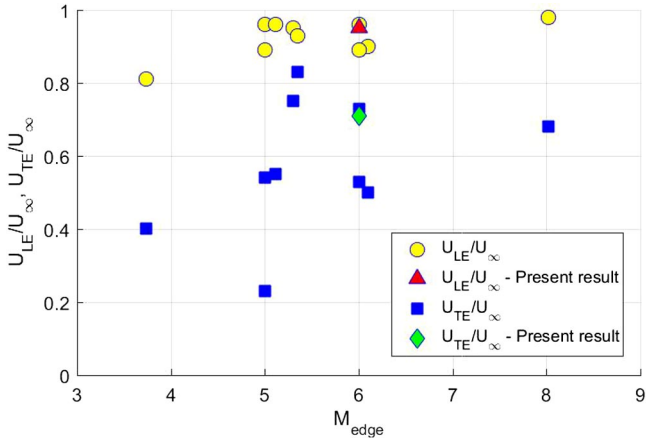

Fig. 11 Summary of turbulent spot leading-edge and trailing-edge convective speeds.

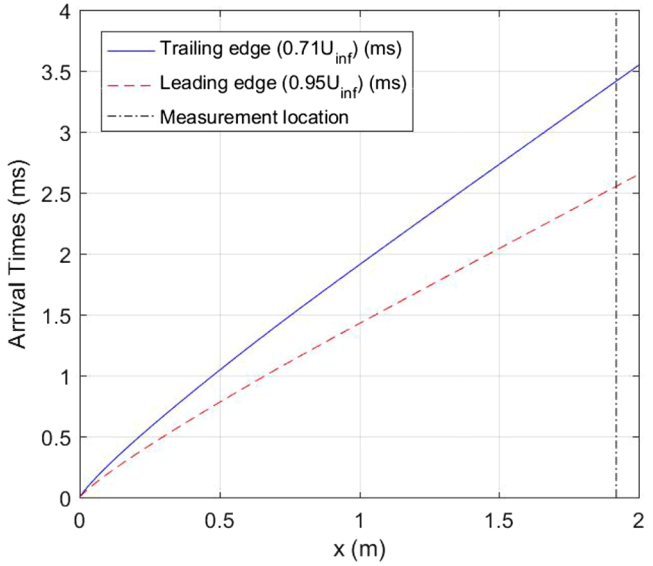

Fig. 12 Traveling times for the leading and trailing edges of the turbulent spot through the nozzle.

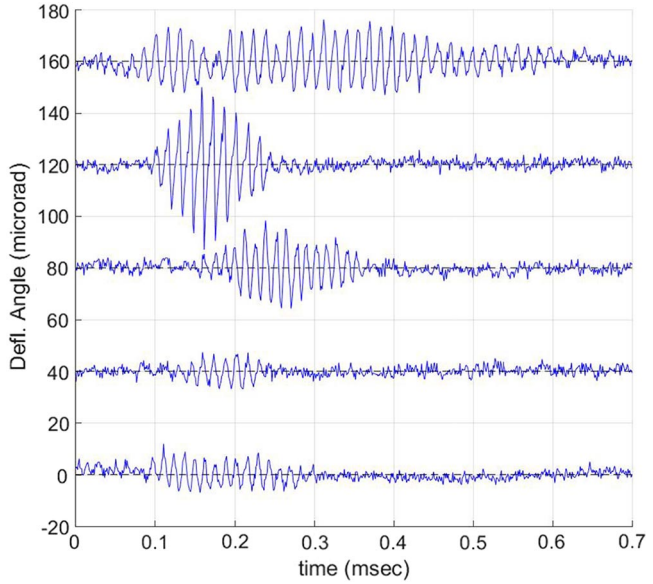

Fig. 13 Examples of deflection-angle time series with fluctuations present. Each successive time series is vertically offset for clarity.

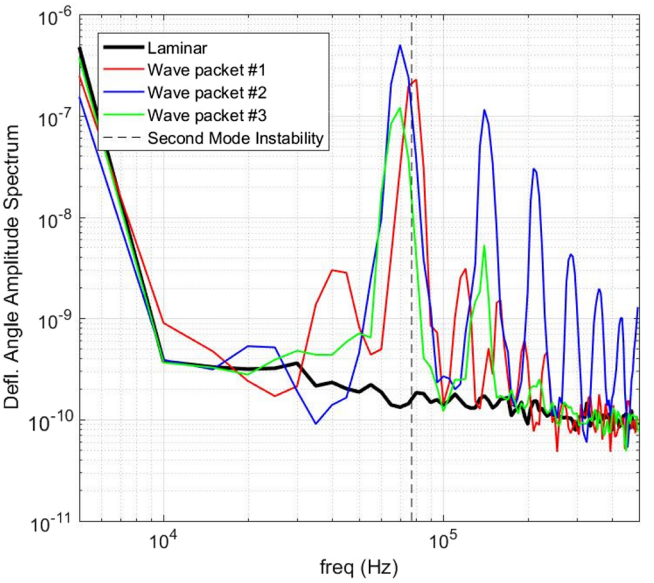

Fig. 14 Deflection angle spectra of the laminar boundary layer (thick black line) and for several narrowband events. Theoretical prediction of the second-mode instability is given as a vertical dashed line.

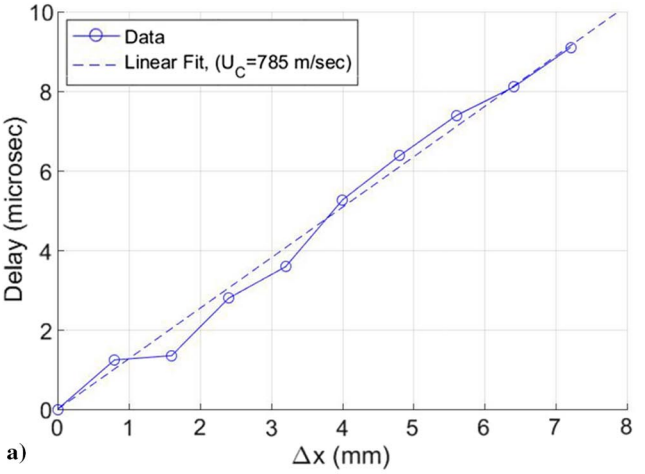

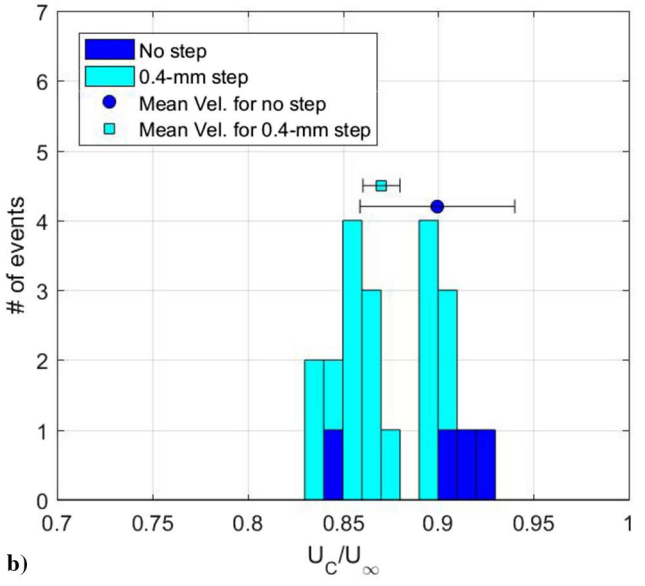

Fig. 15 a) Calculations of the convective speed using time-delayed correlation method. b) Stacked distribution of the convective speed for the narrowband event at the measurement station for no step and downstream of 0.4-mm step. The corresponding average convective speeds with 90% confidence levels are also shown.

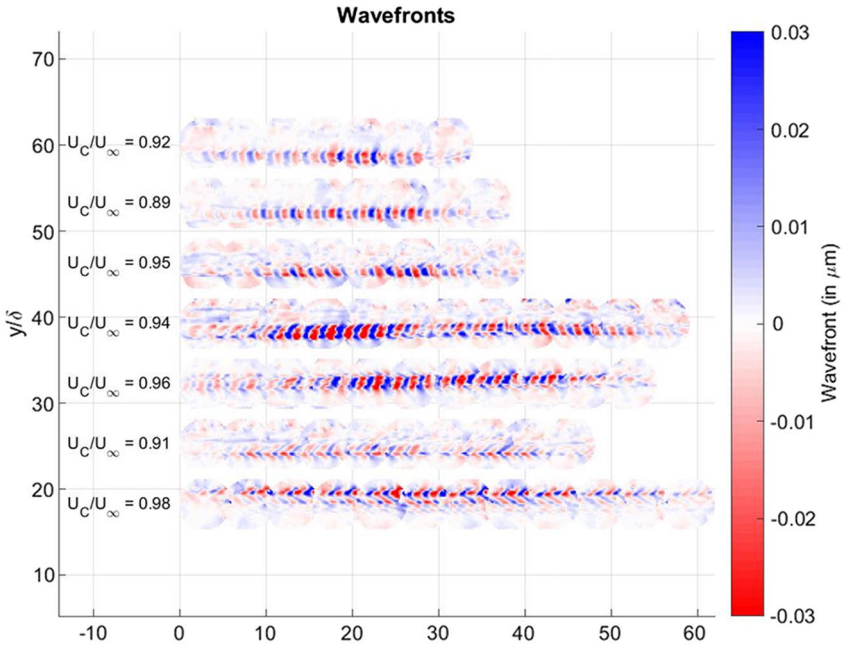

Fig. 16 Examples of stitched 2-D wave fronts corresponding to the second-mode transitional structures and the corresponding convective speeds. Wave fronts are vertically offset for clarity. Flow goes from left to right.

until the correlation in the overlap region is maximized. The resulting shifted wave fronts are combined to create a larger wave front. The third wave front is added by shifting it relative to the second and the process is repeated until all wave fronts are properly combined.

From the average distance of the spatial shift between consecutive wave fronts, an average convective speed was also computed. Several examples of the spatially reconstructed second-mode structures with the corresponding convective speeds are shown in Fig. 16. The average convective speeds were found to be between 0.9 and 0.95 of the freestream speed, consistent with no-step measurements presented in Fig. 15. Note that the overall amount of aero-optical distortions during these events is fairly small, between −0.03 and 0.03 μm; nevertheless, the optical setup was sensitive enough to detect these structures. No controlled disturbances were introduced into the boundary layer—these are naturally occurring wave packets. All these extracted structures show the presence of a streamwise-periodic pattern with a spanwise size of approximately 2–3δ and streamwise extent between 30 and 60δ. The streamwise wavelength was found to be between 1.8 and 2.1δ, consistent with the estimates presented earlier. The convective speeds are similar to the ones discussed in Fig. 15.

In most cases, the structure is not significantly distorted nor modestly tilted in the spanwise direction; qualitatively they resemble the early stages of naturally occurring narrowband wave packets, observed in the cited computations and other measurements in [5]. But in the bottom two examples, the structure shows the presence of the oblique disturbances, or "wings," on both spanwise sides of the structure. These wings exhibit an unusual "reverse bow" behavior, as they lead the main body of the structure (the "head"). This shape differs from the results of Casper et al.'s [5] studies in this tunnel using the series of streamwise/spanwise-arranged unsteady pressure sensors, where it was found that the head of the second-mode structure lead the wings in bow-like fashion. The exact reasons of this discrepancy are currently under investigation; however, there are a few noteworthy differences from the previous work. In [5,41], all measurements were performed at lower stagnation pressures (below 157 psi), whereas in the current investigation, the stagnation pressure was 170–175 psi (just below the tunnel's maximum quiet pressure at the time). It seems unlikely that this ∼15% difference in Reynolds number would change the wave packet structure so significantly. As discussed previously, the chances that these disturbances would appear independently on opposite sides of the tunnel are very low. However, it is possible that two adjacent wave packets would develop in tandem and the reverse bow structure is observed at their shared border. Also, the structures could be affected by the varying step height upstream of the window insert. The wave front amplitudes were comparable with the sensitivity of the WFS, making them hard to extract. Casper et al. observed the bow-shaped pressure footprint when controlled disturbances were introduced by a glow discharge (Fig. 16 in [5]); naturally occurring fluctuations were essentially 2-D (Fig. 10 in [5]). Sivasubramanian and Fasel [7] commented that the visibility of oblique structures they observed were "strongly dependent upon the chosen contour level." Perhaps the absence of bow-shaped structures in these results is simply due to their small amplitude in an unforced boundary layer. Furthermore, we were looking for a specific periodic spatial pattern to extract the structures, so it is possible that we found only a particular subset of the structures or only saw the part of the structure that satisfied the search pattern. Nevertheless, numerical simulations by Sivasubramanian and Fasel [7] of transitional second-mode structures on a cone at Mach 6 are qualitatively similar to what was observed in Fig. 16.

V. Conclusions

Direct measurements of aero-optical disturbances imposed by naturally occurring transitional structures in a Mach-6 laminar boundary layer were performed in the Boeing/AFOSR Mach-6 Quiet Tunnel at Purdue University. These transitional structures were observed only at high stagnation pressures, above 150 psi, corresponding to Reynolds numbers greater than 11.5 M/m. Two types of transitional structures were nonintrusively studied: turbulent spots (or bursts) and second-mode instability waves. For turbulent spots, analysis of the aero-optical data gave a statistical distribution of the spot durations; the mean value was found to about 1.4 ms, placing the origin of the turbulent spot in the nozzle throat. The spots engulfed the full test section at the measurement location, with both the leading and the trailing edges being approximately axisymmetric. The ensemble-averaged aero-optical spectrum revealed that the boundary layer inside the turbulent spot resembles the fully turbulent boundary layer. Detailed measurements of aero-optical distortions during the turbulent spot event show that the boundary layer is about 50% of the thickness of the fully turbulent boundary layer. It is the thickest in the beginning of the spot and decreases toward its end. By performing cross-correlations between wave fronts, the convective speeds of turbulent structures inside the spot were also determined; they had a

largest speed of 0.95–0.97U_∞ in the beginning of the spot, with a gradual decrease to 0.92U_∞ by the end of it.

The optical distortions created by a conical Mach wave, generated by the moving trailing edge of the turbulent spot, were observed. Based on the direct measurements of the location of the conical-shock tip relative to the trailing edge, the speed of the trailing edge of the turbulent spot was found to be 0.7U_∞.

The second type of the observed transitional structures is suspected to be second-mode-instability wave packets. They are characterized by a predominant narrowband frequency of 65–80 kHz, which agrees with the theoretically predicted frequency of $0.5U_\infty/\delta$. The convective speeds were directly measured by cross-correlating aero-optical distortions, with the mean speed of 0.9U_∞; the average spatial wavelength was found to be 1.86δ. To study the streamwise/spanwise topology of the structures, sequential wave fronts were stitched together, using the convective frozen field assumption. The structures were found to be fairly narrow, about 2–3δ in the spanwise direction, while extending for 30–60δ in the streamwise direction. Most of them were fairly uniform in the spanwise direction, consistent with the studies by other researchers. An unusual reverse bow pattern was observed in two of them, when the wings of the structure were found to advance relative to the main structure body. Additional measurements should be performed to collect more data and address the origin of the unusual structures.

Overall, direct nonintrusive aero-optical measurements were undoubtedly found to provide very useful information about the transitional structures in the hypersonic laminar boundary layer. We believe it was the first time the aero-optical environment of transitional structures in the wall-normal direction was experimentally studied. Combined with other wall-mounted instruments, it gives important complementary information about the spatial-temporal evolution of the density field inside these structures.

Acknowledgements

The authors would like to thank Steven Schneider of Purdue University for the opportunity to use the BAM6QT to perform these measurements. We would like to express our gratitude to Bradley M. Wheaton of the Johns Hopkins University Applied Physics Laboratory for calculating the nozzle-wall boundary-layer thickness. We also thank Brandon Chynoweth of Purdue University and Amanda Chou of NASA Langley Research Center for their help preparing the experiment.

References

[1] Schneider, S. P., "Laminar-Turbulent Transition on Reentry Capsules and Planetary Probes," *Journal of Spacecraft and Rockets*, Vol. 43, No. 6, 2006, pp. 1153–1173. doi:10.2514/1.22594

[2] Jumper, E. J., and Gordeyev, S., "Physics and Measurement of Aero-Optical Effects: Past and Present," *Annual Review of Fluid Mechanics*, Vol. 49, No. 1, 2017, pp. 419–441. doi:10.1146/annurev-fluid-010816-060315

[3] Wang, M., Mani, A., and Gordeyev, S., "Physics and Computation of Aero-Optics," *Annual Review of Fluid Mechanics*, Vol. 44, No. 1, 2012, pp. 299–321. doi:10.1146/annurev-fluid-120710-101152

[4] Juliano, T. J., "Nozzle Modifications for High-Reynolds-Number Quiet Flow in the Boeing/AFOSR Mach-6 Quiet Tunnel," Ph.D. Thesis, Purdue Univ., West Lafayette, IN, 2006.

[5] Casper, K. M., Beresh, S. J., and Schneider, S. P., "Pressure Fluctuations Beneath Instability Wavepackets and Turbulent Spots in a Hypersonic Boundary Layer," *Journal of Fluid Mechanics*, Vol. 756, 2014, pp. 1058–1091. doi:10.1017/jfm.2014.475

[6] Casper, K. M., "Hypersonic Wind-Tunnel Measurements of Boundary-Layer Pressure Fluctuations," M.S. Thesis, Purdue Univ., West Lafayette, IN, 2009.

[7] Sivasubramanian, J., and Fasel, H. F., "Numerical Investigation of the Development of Three-Dimensional Wavepackets in a Sharp Cone Boundary Layer at Mach 6," *Journal of Fluid Mechanics*, Vol. 756, 2014, pp. 600–649. doi:10.1017/jfm.2014.434

[8] Casper, K. M., Beresh, S. J., Henfling, J. F., Spillers, R. W., Pruett, B., and Schneider, S. P., "Hypersonic Wind-Tunnel Measurements of Boundary-Layer Pressure Fluctuations," AIAA Paper 2009-4054, 2009.

[9] Heitmann, D., Radespiel, R., and Knauss, H., "Experimental Study of Boundary-Layer Response to Laser-Generated Disturbances at Mach 6," *Journal of Spacecraft and Rockets*, Vol. 50, No. 2, 2013, pp. 294–304. doi:10.2514/1.A32281

[10] Heitmann, D., and Radespiel, R., "Simulations of Boundary-Layer Response to Laser-Generated Disturbances at Mach 6," *Journal of Spacecraft and Rockets*, Vol. 50, No. 2, 2013, pp. 305–316. doi:10.2514/1.A32282

[11] Jewell, J., Parziale, N., Leyva, I., and Shepherd, J., "Turbulent Spot Observations Within a Hypervelocity Boundary Layer on a 5-Degree Half-Angle Cone," AIAA Paper 2012-3062, 2012.

[12] Jewell, J. S., Leyva, I. A., and Shepherd, J. E., "Turbulent Spots in Hypervelocity Flow," *Experiments in Fluids*, Vol. 58, No. 4, 2017, p. 32. doi:10.1007/s00348-017-2317-y

[13] Fiala, A., Hillier, R., Mallinson, S. G., and Wijesinghe, H. S., "Heat Transfer Measurement of Turbulent Spots in a Hypersonic Blunt-Body Boundary Layer," *Journal of Fluid Mechanics*, Vol. 555, 2006, pp. 81–111. doi:10.1017/S0022112006009396

[14] Casper, K. M., Beresh, S. J., Henfling, J. F., Spillers, R. W., and Pruett, B. O. M., "High-Speed Schlieren Imaging of Disturbances in a Transitional Hypersonic Boundary Layer," AIAA Paper 2013-0376, 2013.

[15] Casper, K. M., Beresh, S. J., Wagnild, R. M., Henfling, J. F., Spillers, R. W., and Pruett, B. O. M., "Simultaneous Pressure Measurements and High-Speed Schlieren Imaging of Disturbances in a Transitional Hypersonic Boundary Layer," AIAA Paper 2013-2739, 2013.

[16] Laurence, S. J., Wagner, A., and Hannemann, K., "Experimental Study of Second-Mode Instability Growth and Breakdown in a Hypersonic Boundary Layer Using High-Speed Schlieren Visualization," *Journal of Fluid Mechanics*, Vol. 797, 2016, pp. 471–503. doi:10.1017/jfm.2016.280

[17] Schneider, S. P., "Effects of Roughness on Hypersonic Boundary-Layer Transition," *Journal of Spacecraft and Rockets*, Vol. 45, No. 2, 2008, pp. 193–209. doi:10.2514/1.29713

[18] Gordeyev, S., Smith, A. E., Cress, J. A., and Jumper, E. J., "Experimental Studies of Aero-Optical Properties of Subsonic Turbulent Boundary Layers," *Journal of Fluid Mechanics*, Vol. 740, 2014, pp. 214–253. doi:10.1017/jfm.2013.658

[19] Gordeyev, S., Jumper, E. J., and Hayden, T., "Aero-Optics of Supersonic Boundary Layers," *AIAA Journal*, Vol. 50, No. 3, 2012, pp. 682–690. doi:10.2514/1.J051266

[20] Wyckham, C., and Smits, A., "Aero-Optic Distortion in Transonic and Hypersonic Turbulent Boundary Layers," *AIAA Journal*, Vol. 47, No. 9, 2009, pp. 2158–2168. doi:10.2514/1.41453

[21] Smith, A. E., Gordeyev, S., Ahmed, H., Ahmed, A., Wittich, D. J., III, and Paul, M., "Shack–Hartmann Wavefront Measurements of Supersonic Turbulent Boundary Layers in the TGF," AIAA Paper 2014-2493, 2014.

[22] Gordeyev, S., Rennie, R. M., Cain, A. B., and Hayden, T., "Aero-Optical Measurements of High-Mach Supersonic Boundary Layers," AIAA Paper 2015-3246, 2015.

[23] Gordeyev, S., and Juliano, T. J., "Optical Characterization of Nozzle-Wall Mach-6 Boundary Layers," AIAA Paper 2016-1586, 2016.

[24] Tromeur, E., Garnier, E., and Sagaut, P., "Large-Eddy Simulation of Aero-Optical Effects in a Spatially Developing Turbulent Boundary Layer," *Journal of Turbulence*, Vol. 7, No. 1, 2006, pp. 1–28. doi:10.1080/14685240500307389

[25] Tromeur, E., Sagaut, P., and Garnier, E., "Analysis of the Sutton Model for Aero-Optical Properties of Compressible Boundary Layers," *Journal of Fluids Engineering*, Vol. 128, No. 2, 2005, pp. 239–246. doi:10.1115/1.2170128

[26] White, M., and Visbal, M., "Simulation of Aero-Optical Interactions in Transonic Boundary Layers," AIAA Paper 2011-3279, 2011.

[27] Juliano, T. J., Schneider, S. P., Aradag, S., and Knight, D., "Quiet-Flow Ludwieg Tube for Hypersonic Transition Research," *AIAA Journal*, Vol. 46, No. 7, 2008, pp. 1757–1763. doi:10.2514/1.34640

[28] Laufer, J., "Aerodynamic Noise in Supersonic Wind Tunnels," *Journal of the Aerospace Sciences*, Vol. 28, No. 9, 1961, pp. 685–692. doi:10.2514/8.9150

[29] Wheaton, B. M., and Schneider, S. P., "Roughness-Induced Instability in a Hypersonic Laminar Boundary Layer," *AIAA Journal*, Vol. 50, No. 6, 2012, pp. 1245–1256. doi:10.2514/1.J051199

[30] Chou, A., "Mach-6 Receptivity Measurements of Laser-Generated Perturbations on a Flared Cone," Ph.D. Thesis, Purdue Univ., West Lafayette, IN, 2014.

[31] Wheaton, B. M., "Roughness-Induced Instabilities in a Mach-6 Laminar Boundary Layer," Ph.D. Thesis, Purdue Univ., West Lafayette, IN, 2012.

[32] Gordeyev, S., Cress, J. A., Smith, A., and Jumper, E. J., "Aero-Optical Measurements in a Subsonic, Turbulent Boundary Layer with Non-Adiabatic Walls," *Physics of Fluids*, Vol. 27, No. 4, 2015, pp. 1–17. doi:10.1063/1.4919331

[33] Southwell, W. H., "Wave-Front Estimation from Wave-Front Slope Measurements," *Journal of the Optical Society of America*, Vol. 70, No. 8, 1980, pp. 998–1006. doi:10.1364/JOSA.70.000998

[34] Krishnan, L., and Sandham, N. D., "Effect of Mach Number on the Structure of Turbulent Spots," *Journal of Fluid Mechanics*, Vol. 566, 2006, pp. 225–234. doi:10.1017/S0022112006002412

[35] Schneider, S. P., "Hypersonic Laminar-Turbulent Transition on Circular Cones and Scramjet Forebodies," *Progress in Aerospace Sciences*, Vol. 40, No. 1, Feb. 2004, pp. 1–50. doi:10.1016/j.paerosci.2003.11.001

[36] Zanchetta, M. A., and Hillier, R., "Boundary-Layer Transition on Slender Blunt Cones at Hypersonic Speeds," *Proceedings of the 20th International Symposium on Shock Waves*, edited by B. Sturtevant, J. E. Shepherd, and H. G. Hornung, World Scientific, Pasadena, CA, July 1996, pp. 699–704.

[37] Mee, D. J., "Boundary-Layer Transition Measurements in Hypervelocity Flows in a Shock Tunnel," *AIAA Journal*, Vol. 40, No. 8, 2002, pp. 1542–1548. doi:10.2514/2.1851

[38] Jocksch, A., and Kleiser, L., "Growth of Turbulent Spots in High-Speed Boundary Layers on Flat Plate," *International Journal of Heat and Fluid Flow*, Vol. 29, No. 6, 2008, pp. 1543–1557. doi:10.1016/j.ijheatfluidflow.2008.08.008

[39] Sivasubramanian, J., and Fasel, H. F., "Direct Numerical Simulation of a Turbulent Spot in a Cone Boundary-Layer at Mach 6," AIAA Paper 2010-4599, 2010.

[40] Kemnetz, M. R., and Gordeyev, S., "Optical Investigation of Large-Scale Boundary-Layer Structures," AIAA Paper 2016-1460, 2016.

[41] Casper, K., "Pressure Fluctuations Beneath Instability Wave Packets and Turbulent Spots in a Hypersonic Boundary Layer," Ph.D. Thesis, Purdue Univ., West Lafayette, IN, 2012.

J. M. Austin
Associate Editor